

# SRSNetwork: Siamese Reconstruction-Segmentation Networks based on Dynamic-Parameter Convolution

Bingkun Nian<sup>1†</sup>, Fenghe Tang<sup>2†</sup>, Jianrui Ding<sup>3</sup>, Pingping Zhang<sup>4</sup>, Jie Yang<sup>1</sup>, S. Kevin Zhou<sup>2\*</sup>, Wei Liu<sup>1\*</sup>

<sup>1</sup> Institute of Image Processing and Pattern Recognition, Shanghai Jiao Tong University.

<sup>2</sup> School of Biomedical Engineering & Suzhou Institute for Advanced Research, University of Science and Technology of China

<sup>3</sup> School of Computer Science and Technology, Harbin Institute of Technology

<sup>4</sup> School of artificial intelligence, Dalian University of Technology

## Abstract

In this paper, we present a high-performance deep neural network for weak target image segmentation, including medical image segmentation and infrared image segmentation. To this end, this work analyzes the existing dynamic convolutions and proposes dynamic parameter convolution (DPConv). Furthermore, it reevaluates the relationship between reconstruction tasks and segmentation tasks from the perspective of DPConv, leading to the proposal of a dual-network model called the Siamese Reconstruction-Segmentation Network (SRSNet). The proposed model is not only a universal network but also enhances the segmentation performance without altering its structure, leveraging the reconstruction task. Additionally, as the amount of training data for the reconstruction network increases, the performance of the segmentation network also improves synchronously. On seven datasets including five medical datasets and two infrared image datasets, our SRSNet consistently achieves the best segmentation results. The code is released at <https://github.com/fidshu/SRSNet>.

## 1. Introduction

In the past decade, deep learning based methods have achieved significant success in various computer vision tasks including reconstruction [15], segmentation [14], etc. The most common approach to construct deep Convolutional Neural Networks (CNNs) involves stacking multiple convolutional layers and other fundamental layers organized with predefined feature connections. In segmentation tasks, the U-Net [24] architecture, augmented with techniques such as Transformers and dynamic convolutions,

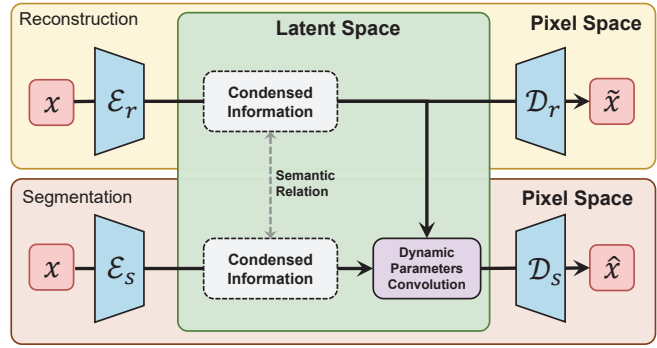


Figure 1. The proposed Siamese Reconstruction-Segmentation (SRS) Networks.  $x$ ,  $\tilde{x}$ ,  $\hat{x}$  respectively represent the input, reconstruction output, and segmentation output.  $\mathcal{E}$  and  $\mathcal{D}$  are encoder and decoder, respectively.

has been widely applied. This research domain is pioneered by Conditional parameterization (CondConv) [34], Dynamic convolutions (DyConv) [8], Omni-Dimension dynamic convolution (ODConv) [17], and Spatial and Channel reconstruction convolution (ScConv) [18]. Typically, in contrast to regular convolutions that apply the same convolutional kernel to all input samples, dynamic convolutions learn linear combinations of different convolutional kernels. The attention weights for these linear combinations are dynamically computed based on input features. And with the help of dynamic convolutions, the accuracy of lightweight CNNs has further improved.

However, the dynamic convolution mentioned above shows the following two obvious flaws: 1) **Not real dynamic**: they all essentially involve the linear combination of different convolutional kernels, and different methods simply compute the combination coefficients differently. These approaches yield satisfactory results when dealing with datasets characterized by relatively simple distribu-

† Equal Contribution \*Corresponding Author

tions. In cases of complex datasets, due to the limited representational capacity of different convolutional kernels, they impede further improvements in network performance. 2) **Poor performance:** these methods heavily rely on the number of convolutional kernels and the computation of combination coefficients, leading dynamic convolution techniques into a predicament where they mainly improve the performance by stacking more kernels and expanding the network size.

These limitations are further exacerbated in the context of weak segmentation tasks, such as medical image segmentation and infrared image segmentation. For instance, in medical and infrared images segmentation tasks, the features of the data are highly complex due to the absence of texture, size, shape, and other characteristics that usually exist in natural images. To handle the problem mentioned above, we propose **Dynamic-Parameter Convolution (DPConv)**. DPConv generates adaptive dynamic-parameter kernels based on the data distribution of input features. Based on the DPConv, we further propose a novel network architecture named as Reconstruction-Segmentation (RS) architecture. This architecture leverages dynamic-parameter kernels to translate segmentation problems into reconstruction problems. In addition, we further show the connection between the low-level reconstruction task and the high-level segmentation task, and we formulate the reconstruction task and the segmentation task as a dual problem, denoted as **Siamese Reconstruction-Segmentation Network (SRSNet)** (shown in Fig. 1). This signifies that more intricate segmentation problems can be approached from a reconstruction perspective. Overall, the contributions of this paper are as follows:

1. We propose a new Dynamic-Parameter Convolution operator named DPConv, and it can adapt to the data distribution of input features, which can significantly boost the network performance.
2. A novel siamese network named SRSNet is further proposed based on the DPConv module. We jointly formulate the reconstruction task and the segmentation task in one network. We further demonstrate that SRSNet can boost the segmentation performance via more training data of the reconstruction task instead of increasing the training data of the segmentation, and this surprising relation between the two tasks is seldom explored by existing works.
3. We apply our method to infrared image segmentation of two datasets and medical image segmentation of five datasets. Through comprehensive experimental results with 16 state-of-art results, we show that our method is able to achieve state-of-the-art performance.

The rest of this paper are as follows: Sec. 2 is devote to the related work. We introduce our SRSNet in Sec. 3. The experiment setting is listed in Sec. 4. And We evaluate the

effectiveness of our method on several weak target datasets and compare it against many state-of-the-art approaches in Sec. 5. The conclusion of this paper is in Sec. 6.

## 2. Related Work

### 2.1. Dynamic Convolutional Neural Networks

By dynamically computing the combination coefficients of convolutional kernels, the neural network exhibits adaptability. This method demonstrates significant potential in increasing model capacity and generalization. Hypernetworks [11] employ a smaller network to generate weights for a larger recursive network. WeightNet [20] attaches grouped fully connected layers to obtain feature vectors from squeeze-and-excitation (SE) blocks, generating weights for CNNs used in image segmentation. Lin et al. [19] modify convolutional layers with gate modules guided by global context, while Quader et al. [23] directly modify weights themselves using SE blocks or simple activation functions conditioned on the convolutional weight size. ODConv [17] aims to address the limitations of dynamic convolutions [8, 34]. In contrast, dynamic-parameter convolution is designed to comprehensively address the dynamic convolutional kernel problem, enabling each parameter of the convolutional kernel to be dynamically determined by the input features, rather than being limited to the combination of different static convolutional kernels. As we will show in our experimental part, our DPConv can deliver superior performance over existing dynamic convolutions [8, 17, 18, 34].

### 2.2. Network Structures for Segmentation Tasks

In the field of weak image segmentation including infrared weak image and medical image, any innovations regarding network structures have been proposed. Among these innovations, one of the most prominent approaches in the field of medical image segmentation is TransUnet [7]. TransUnet combines the Transformer [29] and CNNs architectures to form a robust encoder for 2D medical image segmentation. Similar to TransUnet, Medical Transformer [28] and Transfuse [37] harness the complementarity of Transformers and CNNs to improve the segmentation capabilities of their models. Presently, various combinations of Transformers and CNNs are applied in multi-modal brain tumor segmentation [31] and 3D segmentation [33]. Furthermore, pure Transformers have demonstrated remarkable potentials in medical image segmentation [6].

However, the above-mentioned networks focus solely on improving their own structures under segmentation tasks. Nevertheless, there exists a connection between different tasks, implying that we can combine segmentation tasks with reconstruction tasks to enhance network performance from a different perspective. This is what we will introduce:

dynamic-parameter convolution and SRSNetwork.

### 3. Siamese Reconstruction-Segmentation Network Based on Dynamic-Parameter Convolution

In order to improve the performance of segmentation networks, we propose the dynamic-parameter convolution and further show the connection between the low-level reconstruction task and the high-level segmentation task. The overall structure including construction of DPConv and the RS architecture will be introduced in details.

#### 3.1. Overall of Network Architecture

The Siamese Reconstruction-Segmentation network (SRSNetwork) is illustrated as a whole in Fig. 2. The upper part is specifically crafted for the reconstruction task, whereas the lower part is designed for the segmentation task. DPConv builds the connection between two parts. As shown in Fig. 2,  $x_r, x_s$  contains ResBlock [12] and CBAM [32]. The encoder-decoder structure is enhanced from DNANet [16]. Following the encoder-decoder phase, an improved fusion module named BLAM from ALCNet [10] is employed to integrate high-level semantic information with low-level detailed information.

#### 3.2. Dynamic-Parameter Convolution

In order to adapt to various changes in data distribution, many methods related to dynamic convolutions have been proposed such as CConv [34], Dyconv [8] and OD-Conv [17]. their mathematical descriptions can be summarized as follows:

$$\omega = \sum_{i=1}^n \sum_{j=1}^n \alpha_{ji} \omega_i \quad (1)$$

where  $\omega, \alpha_{ji}, \omega_i$  are new kernel, combination coefficient and fixed sets of convolutional kernels.

Both DyConv [8] and OD-Conv [17] utilize a fixed number of kernels  $\omega_i$ , with the only difference being the number of coefficient sets. And the difference is that DyConv generates one set, while OD-Conv generates four sets.

Although DyConv and OD-Conv replace fixed convolutions with a series of convolutions, they fundamentally rely on a finite set of fixed convolutional kernels once the network converges. The weights can only adapt to a fixed number of situations.

Therefore, convolutional kernels need to break the limitations of a fixed number and seek a new method to extend adaptability. To this end, we propose our dynamic-parameter convolution (DPConv) shown in Fig. 3, DPConv comprises of two elements: the lower part signifies semantic information, while the upper part portrays the process of generating kernel parameters.

After presenting the schematic diagram of DPConv, we also provide its mathematical description. Given that the information in the segmentation task is denoted as  $X$ , and the information in the reconstruction task is denoted as  $Y$ , with a transformation operation  $\psi$ , the dynamic-parameter convolution process can be described by the following formula:

$$DPConv(X, Y) = Conv2d(\psi_1(X), \psi_2(\gamma(Y))) \quad (2)$$

$\gamma$  represents the combination of convolution, avg-pooling, and convolution operations. In this process, each convolutional kernel parameter will be dynamically generated.

To perform the DPConv operation, the convolutional kernel must possess specific parameters: the desired number of target channels is represented as  $M$ , the kernel size is indicated by  $K$ , and the output channels are denoted as  $N$ . The total number of parameters to generate can be expressed as  $n = M \times N \times K^2$ . Thus, in order to generate  $n$  parameters, we choose to construct a one-dimensional vector  $\theta_n$  with size  $n$ .

To get  $\theta_n$ , the semantic feature  $Y \in R^{z=C \times H \times W}$  needs to be translated to one-dimensional vector  $\theta_n$ . However, if we directly convert  $Y$  into  $\theta_n$  using average operations, it will lead to non-convergence of the network. Given reconstruction information input  $Y$ , the semantic translation  $\psi_2$  can be described as:

$$\psi_2(Y) = \sigma_{kernel=1}^{z \Rightarrow n}(\delta(\sigma_{kernel=1}^{z \Rightarrow z}(Y))) \quad (3)$$

Therefore, in Eq. 3, we first employ one  $1 \times 1$  convolution  $\sigma_{kernel=1}^{z \Rightarrow z}$  and adaptive AvgPool  $\delta$  to adjust the channel dimensionality. Then, we use another  $1 \times 1$  convolution  $\sigma_{kernel=1}^{z \Rightarrow n}$  to reshape feature from  $Y$  to  $\theta_n$  and change channels from  $z$  to  $n$ .

#### 3.3. Reconstruction-Segmentation Structure

Now, We have presented the structure of DPConv in Fig. 3. The key question of constructing network comes out: *how to establish a relationship between two tasks (reconstruction and segmentation) using DPConv?* Addressing how the associated network can enhance performance remains a highly challenging question with no existing research in this domain.

In order to solve this challenging question, we utilize the DPConv as the connection between the low-level reconstruction task and the high-level segmentation task (shown in Fig. 2). Reconstruction-Segmentation forms a dual tasks, with the upper and lower parts representing dual networks.

Within the dual networks, DPConv plays a pivotal role. It is clear that DPConv relies on two primary sources of information originating from the reconstruction task and the segmentation task. However, it is essential to note that this does not imply that their structures are entirely identical.

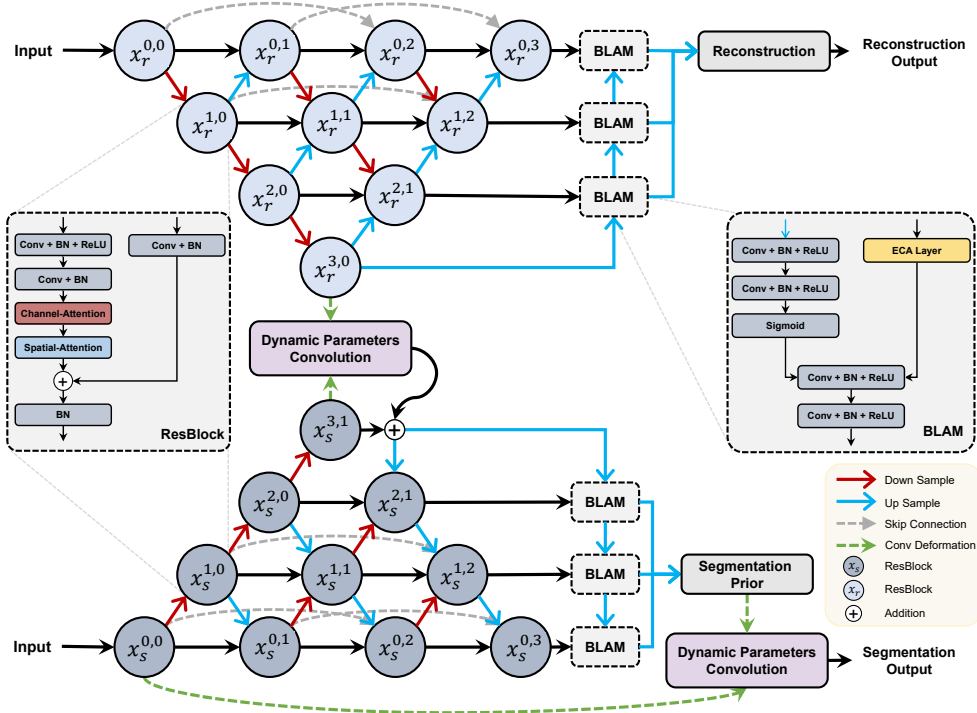


Figure 2. The schematic diagram of the SRSNetwork illustrates a unified structure consisting of two tasks: reconstruction and segmentation. The upper part of the network is dedicated to the reconstruction task, while the lower part is designed for the segmentation task. The connection between two tasks is facilitated by the dynamic-parameter convolution.

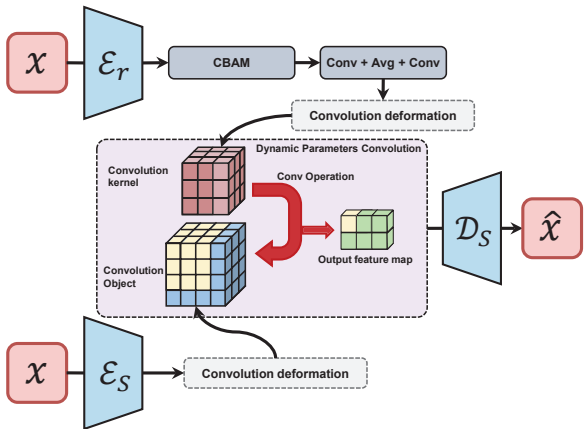


Figure 3. The DPCConv structure comprises two components.  $\mathcal{E}_r$  and  $\mathcal{E}_s$  are the encoder of the reconstruction and segmentation networks.  $\mathcal{D}_s$  is the decoder of segmentation network. The upper structure provides information for generating dynamic-parameter kernel component and the lower provides input data convoluted.

There are some differences between the reconstruction network and segmentation network, primarily manifested in two aspects:

1) **Quantity of ResBlock:** The reconstruction network

primarily provides highly condensed information, which is mainly determined by the convolutional parameters within the ResBlock. Therefore, in the reconstruction network, there is no need to stack basicblocks excessively. Conversely, the segmentation task requires more convolutions to process the input, necessitating a larger number of ResBlocks.

2) **Training Setting:** Unlike segmentation tasks, reconstruction task is essentially an unsupervised task and does not require any labels. To provide more accurate and comprehensive information, we can easily obtain a large volume of relevant images and use them to train the reconstruction network. In contrast, the segmentation network is trained following conventional network training procedures.

The specific network configuration parameters are outlined in Table 1. One crucial point to emphasize is as follows: On the one hand, reconstruction, being an unsupervised task, allows us to gather a substantial amount of similar and even dissimilar images as training data. This enables us to create a reconstruction network that possesses robust adaptability and is not constrained by specific task types. On the other hand, as the dual task of segmentation, the performance of reconstruction can improve without altering the structure, framework, or training strategy of any segmentation task. Consequently, segmentation can, to a



Figure 4. Images from different dataset. We can see that the targets to be segmented basically do not contain valid internal information, and the remaining valid information is also less different from external clutters. When the network judges, we believe that it depends more on the distribution, and this distribution requires a larger window to capture.

Network	Quantity	Training Parameters	
		Ratio	Additional
Reconstruction	[5,5,5,5]	All for training	Yes
Segmentation	[6,8,12,6]	Usual Training	No

Table 1. Settings for reconstruction and segmentation networks

certain extent, overcome real-world constraints such as limited data samples. Thus, we think that the RS structure has the potential to aid segmentation tasks in surmounting the challenges posed by single-task limitations.

More importantly, the above characteristics imply that we can also make certain modifications to the design of CNNs. Within a certain range, lightweight and performance are no longer contradictory issues. In the case of performance degradation due to lightweight segmentation design, we can compensate by increasing the training data for the reconstruction task.

## 4. Experiment Setting

### 4.1. Dataset

As shown in Fig. 4, the datasets used in this study comprises two main categories, namely medical image and infrared image. In medical image dataset, three modalities medical images are selected: CT, ultrasound and dermoscopy image. In infrared images, small target image dataset is selected.

The CT image category comprises datasets such as Synapse [3], while the ultrasound image category encompasses BUS [38], BUSI [5] and TNSCUI [4] dataset. Furthermore, the dermoscopy image category includes the ISIC2018 [1] dataset, and the infrared small target image category encompasses the SIRST [2] and NUDT-KBT19 [13] datasets.

We randomly split each of the six image datasets (BUS, BUSI, TNSCUI, ISIC2018, SIRST, NUDT-KBT19) into training and validation sets three times, using a 70/30 split for training and validation. The setting of CT Dataset is the same as that of TransUnet [7].

### 4.2. Evaluation Metrics and Comparison Methods

In this study, we primarily utilize three widely recognized evaluation metrics to assess the performance of our approach. These metrics include Intersection over Union (IoU) and F1 score for the BUS, BUSI, TNSCUI, ISIC2018, SIRST, NUDT-KBT19 datasets; hausdorff distance (HD95), Dice and mIoU coefficient for the Synapse datasets.

To evaluate the performance of weak target image segmentation, We selected 16 currently popular target segmentation models, including: U-Net [24], CMU-Net [26], nnUNet [14]; Transformer-based: TransUnet [7], MedT [28], SwinUnet [6], MobileViT [21], EdgeViT [22], RepViT [30], EMO [35], lightweight: UNeXt [27], EGE-Net [25]. In infrared small target image, we compared our network with ALCNet [10], ACM [9], AGPCNet [36] and DNANet [16].

### 4.3. Loss Function and Implement Details

The reconstruction loss  $\mathcal{L}_r$  is L2 loss and defined as follows:

$$\mathcal{L}_r = \frac{1}{2N} \sum_{i=1}^N (\tilde{y}_i - y_i)^2 \quad (4)$$

where  $\tilde{y}_i$  is the reconstruction image and  $y_i$  is the origin image. The segmentation loss  $\mathcal{L}_s$  between the predicted  $y$  and ground truth  $\hat{y}$  is defined as a combination of the binary cross entropy (BCE) and dice loss (Dice):

$$\mathcal{L}_s = 0.5 \times BCE(y, \hat{y}) + DICE(y, \hat{y}) \quad (5)$$

we resize all training cases of seven datasets to  $256 \times 256$  and apply random rotation and flip for simple data augmentations. In addition, we use the SGD optimizer with a weight decay of  $1e^{-4}$  and a momentum of 0.9 to train the networks. The initial learning rate is set to 0.01, and the poly strategy is used to adjust the learning rate. The batch size is set to 8 and the training epochs are 300. All the experiments are conducted with a single NVIDIA GeForce RTX4090 GPU.

The detailed settings of networks are shown in Table. 1. It's important to note that we first train the reconstruction

Network	#Pub	Ultrasound Datasets						Dermoscopy Datasets	
		BUS		BUSI		TNSCUI		ISIC2018	
		IoU	F1	IoU	F1	IoU	F1	IoU	F1
<i>natural image network</i>									
MobileViT-s [21]	ICLR'22	82.57±1.38	89.99±1.17	64.28±3.78	74.68±3.81	71.64±0.28	81.60±0.25	80.12±0.42	87.89±0.43
EdgeViT-s [22]	ECCV'22	81.32±1.23	89.13±0.99	61.12±3.69	71.79±4.00	68.74±0.29	79.19±0.36	79.06±0.56	87.06±0.55
RepViT-m3 [30]	ArXiv'23	76.51±1.38	85.79±1.12	56.07±3.51	67.62±3.98	66.21±0.66	77.09±0.49	78.34±0.61	86.62±0.48
EMO-6m [35]	ICCV'23	84.89±0.86	91.58±0.63	67.50±4.26	77.71±4.23	74.02±0.39	83.53±0.25	81.31±0.73	88.74±0.57
<i>weak target network</i>									
U-Net [24]	MICCAI'15	86.73±1.41	92.46±1.17	68.61±2.86	76.97±3.10	75.88±0.18	84.24±0.07	82.18±0.87	89.97±0.52
MedT [28]	MICCAI'21	80.81±2.77	88.78±1.96	63.36±1.56	73.37±1.63	71.00±2.68	80.87±2.16	81.79±0.94	89.74±0.53
UNeXt [27]	MICCAI'22	84.73±1.23	91.20±0.94	65.04±2.71	74.16±2.84	71.04±0.17	80.46±0.16	82.10±0.88	89.93±0.46
EGE-Unet [25]	MICCAI'23	84.72±1.28	91.72±0.75	58.90±2.97	74.11±2.34	74.47±0.43	85.36±0.28	82.19±1.31	<u>90.22±0.79</u>
CMU-Net [26]	ISBI'23	87.18±0.59	92.89±0.41	71.42±2.65	79.49±2.92	77.12±0.49	85.35±0.50	82.16±1.06	89.92±0.62
TransUnet [7]	ArXiv'21	87.35±1.24	92.88±0.88	71.39±2.37	79.85±2.59	77.63±0.14	85.76±0.20	83.17±1.25	<b>90.57±0.72</b>
SwinUnet [6]	ECCV'22	85.27±1.24	91.99±0.75	63.59±4.96	76.94±4.12	75.77±1.29	85.82±0.91	82.15±1.44	89.98±0.87
nnUNet [14]	Nature method'21	87.51±1.01	<u>93.02±0.73</u>	<u>72.11±3.51</u>	<u>80.09±3.77</u>	78.99±0.14	<u>86.85±0.15</u>	<b>83.31±0.59</b>	89.84±0.50
<b>SRSNet</b>	CVPR'24	<b>88.29±0.73</b>	<b>93.44±0.61</b>	<b>74.47±2.23</b>	<b>82.57±2.12</b>	<b>79.33±0.43</b>	<b>87.02±0.33</b>	<u>83.16±0.24</u>	89.72±0.12

Table 2. Result on Ultrasound and Dermoscopy Datasets. **val** (bold) / val (underline) : top method / second

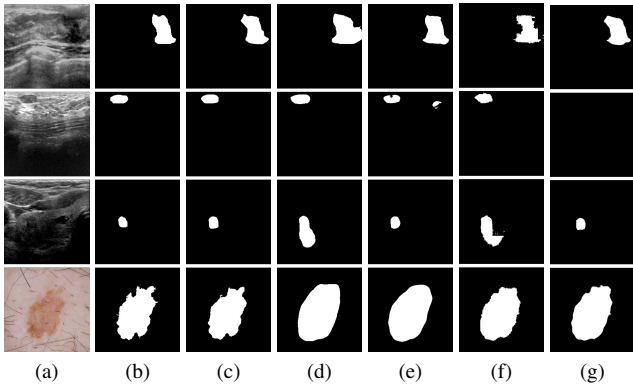


Figure 5. Visualization Top Five Results on Medical Ultrasound and Dermoscopy Datasets. (a) Original Medical Image (b) Ground Truth (c) SRS (d) nnUNet (e) TransUnet (f) Swin-Unet (g) CMU-Net

part, and then, during the training of the segmentation part, the reconstruction part does not participate in the backpropagation to update the weights.

## 5. Comparison with Other Segmentation Methods

### 5.1. Experiments on Medical Images

In Fig. 5 and Fig. 6, we present results of various algorithms. The visual representation clearly demonstrates that the proposed SRSNet surpasses other state-of-art algorithms in terms of visual quality. To ensure a robust evaluation, the subsequent sections provide an in-depth analysis of quantitative results in terms of medical image and infrared small target images.

#### 5.1.1 Experiments on Ultrasound Tumor Images

In ultrasound image segmentation tasks (BUS, BUSI, TNSCUI), our proposed SRSNet is compared with other state-of-art networks in Table. 2. Quantitative results show that our SRSNet achieves the best performance.

nnUNet (proposed in [14] nature method) achieves the second highest IoU and F1 scores. However it exhibits long inference times that can be computationally inconvenient. In contrast, our algorithm not only attains higher accuracy than nnUNet but also avoids the shortcomings of nnUNet.

One important point should be noted is that the networks in Table. 2 can be categorized into two types: specialized network and universal network. This distinction is also observable in the subsequent experiments. Universal networks demonstrate adaptability across different datasets and exhibit superior performance. On the other hand, excel primarily in specific tasks. In fact, the universal networks is extremely rare and hard to design.

Fortunately, with the help of our DPConv and RS structure, SRSNet successfully becomes universal network. This means SRSNet has a higher value than nnUNet and TransUnet for its highest performance.

The success of SRSNet demonstrates that, with the assistance of DPConv, we can unite two distinct tasks, enhancing the performance of one task's network by leveraging the network of the other task without altering the structure and parameters of networks. For instance, the reconstruction task and the segmentation task represent a pair of dual tasks.

#### 5.1.2 Experiments on Dermoscopy Images

In this set of experiments, we focus on the challenging task of skin cancer segmentation under natural light conditions. As shown in Table. 2, our method, SRSNet, still exhibits the

Network	mIoU↓	Dice↑	HD95↓	Synapse (Metrics (%))							
				Aorta	Gallbladder	Kidney (L)	Kidney (R)	Liver	Pancreas	Spleen	Stomach
<i>natural image network</i>											
MobileViT-s [21]	41.66	55.57	30.81	24.63	16.58	50.94	45.85	77.74	17.90	58.80	40.83
EdgeViT-s [22]	36.86	50.68	31.82	21.97	12.23	41.42	38.96	76.43	16.00	50.71	37.16
RepViT-m3 [30]	34.07	47.61	30.69	20.71	7.16	33.56	37.28	74.33	13.28	48.13	38.09
EMO-6m [35]	45.30	59.47	27.68	28.42	22.85	51.88	48.19	79.50	22.19	60.80	48.54
<i>weak target network</i>											
TransUnet [7]	<u>68.33</u>	<u>79.12</u>	<b>23.76</b>	<u>78.47</u>	<u>41.83</u>	<b>75.26</b>	<b>72.59</b>	<u>89.90</u>	<u>44.87</u>	<u>80.07</u>	<b>63.68</b>
Swin-Unet [6]	62.42	74.13	28.54	70.43	35.73	68.58	61.64	88.52	37.01	79.48	57.97
MedT [28]	43.51	55.21	60.06	67.49	1.63	61.82	49.81	36.11	20.26	66.33	44.64
UNeXt [27]	57.22	69.99	41.43	69.35	36.47	63.21	50.45	85.09	28.87	72.34	52.02
<b>SRSNet</b>	<b>69.28</b>	<b>79.80</b>	<u>24.51</u>	<b>80.09</b>	<b>48.97</b>	<u>74.68</u>	<u>71.50</u>	<b>90.80</b>	<b>46.29</b>	<b>80.24</b>	<u>61.71</u>

Table 3. Result on Computed Tomography Datasets. **val** (bold) / val (underline) : top method / second

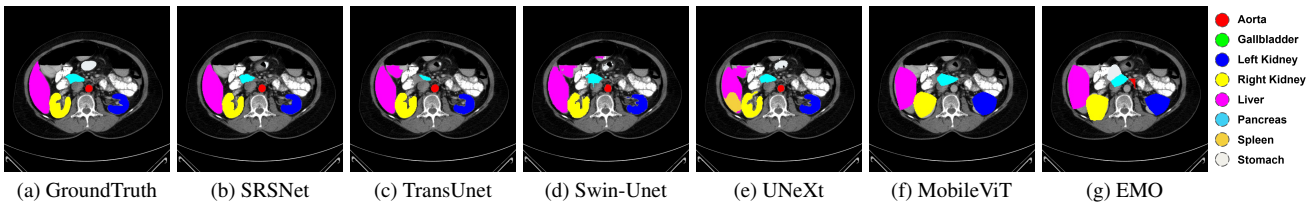


Figure 6. Visualization Top Five Results on Synapse.

wonderful accuracy in skin cancer segmentation. In particular, compared with some networks like EGE-Unet, which is designed for skin cancer, our SRSNet maintains or even improves the performance (1.05% higher than EGE-Unet).

Nowadays, all lightweight Transformers and CNNs achieve relatively favorable results. But it is important to note that the skin cancer dataset contains abundant details such as texture, contrast, and clear edges. Additionally, the distribution of the test data closely aligns with that of the training data, simplifying network training and enabling all networks to perform well in this scenario. However, it is crucial to recognize that such scenarios represent only a small portion of medical segmentation tasks, with the majority involving weak target segmentation, such as ultrasound images and CT images. As depicted in ultrasound datasets, the remaining lightweight models experience significant drops in performance, indicating that their attempts at achieving lightweight design are ultimately unsuccessful.

### 5.1.3 Experiments on Computed Tomography Images

In our comprehensive evaluation, we also perform experiments on CT images. It is essential to note that CT images inherently exist in 3D space, allowing for the application of both 3D and 2D segmentation methods. For this evaluation, we choose the 2D segmentation approach, which involves independently segmenting individual slices of the CT volume.

The evaluation metrics employ for CT images are mIoU, Dice, and HD95. The experimental results are summarized

in Table 3. Notably, apart from the versatile TransUNet and our SRSNet, both transformer-based networks and CNN-based networks experienced a significant decline in performance. For instance, compared to TransUNet, models such as MedT, EdgeViT, and MobileViT, among others, exhibited performance drops of up to 20%. Similarly, CNN based networks also demonstrated a performance decrease of approximately 10%.

These findings underscore the superior performance of our proposed structure, SRSNet, in CT tasks. SRSNet not only achieves the highest accuracy but also showcases improvements in each kind of viscus such as Aorta, Gallbladder. Considering its new structure and fundamental ideal, this further highlights the suitability of our network, ensuring effective medical image segmentation.

### 5.2. Experiments on Infrared Images

Another crucial domain within weak target segmentation is infrared target segmentation. In contrast to medical image datasets, infrared image datasets exhibit more severe challenges, including internal feature scarcity, minimal target pixel occupancy (potentially just a few pixels), and complex backgrounds. Therefore, the segmentation of infrared weak small targets presents a greater challenge for network performance.

In addition to the four state-of-the-art neural network algorithms mentioned earlier, table 4 displays IoU and F1 scores for these algorithms. It is evident that SRSNet achieves the highest segmentation performance on both the SIRST and NUDT-KBT19 datasets. Compared with

Network	# Pub	Type	SIRST		NUDT-KBT19	
			IoU	F1	IoU	F1
AGPCNet [36]	TAES'23	neural	69.25	80.54	84.88	90.80
ACM [9]	WACV'21	neural	72.10	81.42	77.16	86.46
ALCNet [10]	TGRS'21	neural	72.80	83.67	80.22	87.66
DNANet [16]	TIP'22	neural	73.13	83.87	85.66	91.13
<b>SRSNet</b>	CVPR'24	neural	<b>74.67</b>	<b>84.28</b>	<b>86.34</b>	<b>92.62</b>

Table 4. Different Experiment on Infrared Small Target Datasets. **val** (bold) / val (underline) : top method / second

Network	BUS		BUSI		SIRST	
	IoU	F1	IoU	F1	IoU	F1
S+Dyconv[8]	87.60±0.92	93.16±0.54	71.35±4.27	79.80±4.05	71.03	81.70
S+OD-Conv[17]	87.58±0.88	93.16±0.54	70.82±3.01	79.37±3.27	71.70	82.97
S+ScConv[18]	87.43±0.76	93.02±0.58	71.29±3.22	79.85±3.39	71.03	81.83
SRS(DPConv)	<b>88.29±0.73</b>	<b>93.45±0.61</b>	<b>74.47±2.23</b>	<b>82.57±2.12</b>	<b>74.67</b>	<b>84.28</b>

Table 5. Ablation study on Reconstruction task of SRSNet

the current state-of-the-art algorithm DNANet, SRSNet demonstrates a 1.54% improvement on SIRST and a 0.68% improvement on NUDT-KBT19. This indicates that SRSNet can achieve state-of-the-art results in the field of infrared small target segmentation as well.

Taking Table. 4 into consideration, the key contribution of SRSNet lies in its novel structure and its versatility in the area of weak target segmentation. Regardless of the data set taken in various environments (Ultrasound, Dermoscopy, CT or Infrared), it can achieve the current state-of-art effect.

### 5.3. Ablation Study

#### 5.3.1 Role of DPConv

In Table. 5, we conducted ablation experiments on DPConv, considering ScConv[18], DyConv[8], and ODConv[17] as alternative choices. It is evident that the selection of dynamic convolution has a substantial impact on the overall model performance. The results demonstrate that DPConv, as introduced in this paper, outperforms traditional dynamic convolutions by a significant margin. For instance, when examining the BUSI dataset, DPConv exhibits an improvement of 3.18% in IoU and 2.71% in F1 score compared to ScConv[18].

This further corroborates our earlier analysis: in datasets characterized by complexity and poor image quality, conventional dynamic convolutions, owing to their fixed kernel forms, fail to effectively enhance performance and may, in fact, lead to performance degradation even non-convergence (DyConv in SIRST). This indirectly underscores the significance of the DPConv concept presented in this paper.

#### 5.3.2 Role of Reconstruction Task of SRSNet

The experimental results are shown in the Table. 6. We investigate the overall architecture on multiple datasets to ex-

Network	BUS		BUSI		SIRST	
	IoU	F1	IoU	F1	IoU	F1
S Stage	88.22±0.90	93.53±0.57	73.85±2.96	82.00±3.19	73.78	84.25
R+S Stage	<b>88.29±0.73</b>	<b>93.45±0.61</b>	<b>74.47±2.23</b>	<b>82.57±2.12</b>	<b>74.67</b>	<b>84.28</b>

Table 6. Ablation Study on Reconstruction Task of SRSNet

Network	BUS		BUSI		SIRST	
	IoU	F1	IoU	F1	IoU	F1
T dataSet	<b>88.30±0.47</b>	<b>93.59±0.29</b>	73.79±1.85	82.12±1.93	73.19	83.78
T + V dataSet	88.29±0.73	93.45±0.61	<b>74.47±2.23</b>	<b>82.57±2.12</b>	<b>74.67</b>	<b>84.28</b>

Table 7. Ablation study on Reconstruction Data Setting

plore the gain of reconstruction task (R stage) for the segmentation task (S stage) When we add a R stage to the S stage based on DPConv, We found that dynamic convolutions generated by the reconstruction task can bring improvements for segmentation task. This shows that the reconstruction task can use DPConv as a bridge to transfer additional beneficial domain knowledge to the segmentation task, thereby enhancing the network’s representation ability and pattern coverage of the overall data set distribution.

#### 5.3.3 Role of Reconstruction Data Setting

The experimental results are shown in the Table. 7. We conduct ablation study on the impact of reconstruction data setting on segmentation performance during the R stage. We let the R network learn the pattern distribution of different numbers of datasets, that is, only the training set (T dataset) and the complete dataset consisting of training and validation sets (T+V dataset). The phenomena is very fascinating. This trend is not always positively impactful and can vary with changes in the dataset. When dealing with a large dataset, expanding the reconstruction dataset (T+V) yields favorable results. However, the effects are not as pronounced when working with smaller datasets. Nevertheless, this does not diminish the overall value of the approach. As the reconstruction task operates as an unsupervised network, we have the flexibility to readily expand the dataset in a simple and efficient manner. We can even train it on natural images to transform it into a generic image model, thereby enhancing the segmentation task’s generalization and accuracy.

## 6. Conclusion

This paper introduces an innovative weak target segmentation network called SRSNet. SRSNet is a siamese network that combines the task of reconstruction and segmentation. It excels in maintaining high versatility, a low parameter count, and new design concept, all while preserving or even enhancing accuracy in general weak target segmentation tasks including medical and infrared image.

The key contribution of SRSNet lies in its novel structure, design of DPConv and versatility. This novel method



enables us to think about how to improve the performance of a single task from a new perspective. Compared with the current state-of-art universal weak target segmentation network including medical and infrared network, SRSNet successfully achieves the highest performance.

## References

- [1] Isic2018: <https://challenge.isic-archive.com/data/#2018>, . 5
- [2] Sirst: <https://github.com/yimiandai/sirst/tree/master>, . 5
- [3] Synapse: <https://www.synapse.org/#!/synapse:syn3193805/files/>, . 5
- [4] Tnscui: <https://tn-scui2020.grand-challenge.org/dataset/>, . 5
- [5] Walid Al-Dhabyani, Mohammed Gomaa, Hussien Khaled, and Aly Fahmy. Dataset of breast ultrasound images. *Data in brief*, 28:104863, 2020. 5
- [6] Hu Cao, Yueyue Wang, Joy Chen, Dongsheng Jiang, Xiaopeng Zhang, Qi Tian, and Manning Wang. Swin-unet: Unet-like pure transformer for medical image segmentation. In *European conference on computer vision*, pages 205–218. Springer, 2022. 2, 5, 6, 7, 3, 4
- [7] Jieneng Chen, Yongyi Lu, Qihang Yu, Xiangde Luo, Ehsan Adeli, Yan Wang, Le Lu, Alan L Yuille, and Yuyin Zhou. Transunet: Transformers make strong encoders for medical image segmentation. *arXiv preprint arXiv:2102.04306*, 2021. 2, 5, 6, 7, 3, 4
- [8] Yinpeng Chen, Xiyang Dai, Mengchen Liu, Dongdong Chen, Lu Yuan, and Zicheng Liu. Dynamic convolution: Attention over convolution kernels. In *Proceedings of the IEEE/CVF conference on computer vision and pattern recognition*, pages 11030–11039, 2020. 1, 2, 3, 8
- [9] Yimian Dai, Yiquan Wu, Fei Zhou, and Kobus Barnard. Asymmetric contextual modulation for infrared small target detection. In *Proceedings of the IEEE/CVF Winter Conference on Applications of Computer Vision*, pages 950–959, 2021. 5, 8
- [10] Yimian Dai, Yiquan Wu, Fei Zhou, and Kobus Barnard. Attentional local contrast networks for infrared small target detection. *IEEE Transactions on Geoscience and Remote Sensing*, 59(11):9813–9824, 2021. 3, 5, 8
- [11] David Ha, Andrew Dai, and Quoc V. Le. Hypernetworks, 2016. 2
- [12] Kaiming He, Xiangyu Zhang, Shaoqing Ren, and Jian Sun. Deep residual learning for image recognition. In *Proceedings of the IEEE conference on computer vision and pattern recognition*, pages 770–778, 2016. 3
- [13] Bingwei Hui, Zhiyong Song, Hongqi Fan, P Zhong, W Hu, X Zhang, J Ling, H Su, W Jin, Y Zhang, et al. A dataset for infrared detection and tracking of dim-small aircraft targets under ground/air background. *China Sci. Data*, 5(3):291–302, 2020. 5
- [14] Fabian Isensee, Paul F Jaeger, Simon AA Kohl, Jens Petersen, and Klaus H Maier-Hein. nnu-net: a self-configuring method for deep learning-based biomedical image segmentation. *Nature methods*, 18(2):203–211, 2021. 1, 5, 6, 4
- [15] Xiangtao Kong, Hengyuan Zhao, Yu Qiao, and Chao Dong. Classr: A general framework to accelerate super-resolution networks by data characteristic. In *Proceedings of the IEEE/CVF conference on computer vision and pattern recognition*, pages 12016–12025, 2021. 1
- [16] Boyang Li, Chao Xiao, Longguang Wang, Yingqian Wang, Zaiping Lin, Miao Li, Wei An, and Yulan Guo. Dense nested attention network for infrared small target detection. *IEEE Transactions on Image Processing*, 32:1745–1758, 2022. 3, 5, 8
- [17] Chao Li, Aojun Zhou, and Anbang Yao. Omni-dimensional dynamic convolution. In *International Conference on Learning Representations*, 2022. 1, 2, 3, 8
- [18] Jiafeng Li, Ying Wen, and Lianghua He. Sconv: Spatial and channel reconstruction convolution for feature redundancy. In *Proceedings of the IEEE/CVF Conference on Computer Vision and Pattern Recognition*, pages 6153–6162, 2023. 1, 2, 8
- [19] Xudong Lin, Lin Ma, Wei Liu, and Shih-Fu Chang. Context-gated convolution. In *Computer Vision—ECCV 2020: 16th European Conference, Glasgow, UK, August 23–28, 2020, Proceedings, Part XVIII 16*, pages 701–718. Springer, 2020. 2
- [20] Ningning Ma, Xiangyu Zhang, Jiawei Huang, and Jian Sun. Weightnet: Revisiting the design space of weight networks. In *European Conference on Computer Vision*, pages 776–792. Springer, 2020. 2
- [21] Sachin Mehta and Mohammad Rastegari. Mobilevit: light-weight, general-purpose, and mobile-friendly vision transformer. *arXiv preprint arXiv:2110.02178*, 2021. 5, 6, 7, 2, 3, 4
- [22] Junting Pan, Adrian Bulat, Fuwen Tan, Xiatian Zhu, Lukasz Dudziak, Hongsheng Li, Georgios Tzimiropoulos, and Brais Martinez. Edgevits: Competing light-weight cnns on mobile devices with vision transformers. In *European Conference on Computer Vision*, pages 294–311. Springer, 2022. 5, 6, 7, 2, 3, 4
- [23] Niamul Quader, Md Mafijul Islam Bhuiyan, Juwei Lu, Peng Dai, and Wei Li. Weight excitation: Built-in attention mechanisms in convolutional neural networks. In *Computer Vision—ECCV 2020: 16th European Conference, Glasgow, UK, August 23–28, 2020, Proceedings, Part XXX 16*, pages 87–103. Springer, 2020. 2
- [24] Olaf Ronneberger, Philipp Fischer, and Thomas Brox. U-net: Convolutional networks for biomedical image segmentation. In *Medical Image Computing and Computer-Assisted Intervention—MICCAI 2015: 18th International Conference, Munich, Germany, October 5-9, 2015, Proceedings, Part III 18*, pages 234–241. Springer, 2015. 1, 5, 6, 4
- [25] Jiacheng Ruan, Mingye Xie, Jingsheng Gao, Ting Liu, and Yuzhuo Fu. Ege-unet: an efficient group enhanced unet for skin lesion segmentation. In *International Conference on Medical Image Computing and Computer-Assisted Intervention*, pages 481–490. Springer, 2023. 5, 6
- [26] Fenghe Tang, Lingtao Wang, Chunping Ning, Min Xian, and Jianrui Ding. Cmu-net: a strong convmixer-based medical ultrasound image segmentation network. In *2023 IEEE 20th International Symposium on Biomedical Imaging (ISBI)*, pages 1–5. IEEE, 2023. 5, 6, 1, 4
- [27] Jeya Maria Jose Valanarasu and Vishal M Patel. Un-ext: Mlp-based rapid medical image segmentation network.

- In *International Conference on Medical Image Computing and Computer-Assisted Intervention*, pages 23–33. Springer, 2022. [5](#), [6](#), [7](#), [1](#), [3](#), [4](#)
- [28] Jeya Maria Jose Valanarasu, Poojan Oza, Ilker Hacihaliloglu, and Vishal M Patel. Medical transformer: Gated axial-attention for medical image segmentation. In *Medical Image Computing and Computer Assisted Intervention–MICCAI 2021: 24th International Conference, Strasbourg, France, September 27–October 1, 2021, Proceedings, Part I 24*, pages 36–46. Springer, 2021. [2](#), [5](#), [6](#), [7](#), [3](#), [4](#)
- [29] Ashish Vaswani, Noam Shazeer, Niki Parmar, Jakob Uszkoreit, Llion Jones, Aidan N Gomez, Łukasz Kaiser, and Illia Polosukhin. Attention is all you need. *Advances in neural information processing systems*, 30, 2017. [2](#)
- [30] Ao Wang, Hui Chen, Zijia Lin, Hengjun Pu, and Guiguang Ding. Repvit: Revisiting mobile cnn from vit perspective. *arXiv preprint arXiv:2307.09283*, 2023. [5](#), [6](#), [7](#), [2](#), [3](#), [4](#)
- [31] Wenxuan Wang, Chen Chen, Meng Ding, Hong Yu, Sen Zha, and Jianguyun Li. Transbts: Multimodal brain tumor segmentation using transformer. In *Medical Image Computing and Computer Assisted Intervention–MICCAI 2021: 24th International Conference, Strasbourg, France, September 27–October 1, 2021, Proceedings, Part I 24*, pages 109–119. Springer, 2021. [2](#)
- [32] Sanghyun Woo, Jongchan Park, Joon-Young Lee, and In So Kweon. Cbam: Convolutional block attention module. In *Proceedings of the European conference on computer vision (ECCV)*, pages 3–19, 2018. [3](#)
- [33] Yutong Xie, Jianpeng Zhang, Chunhua Shen, and Yong Xia. Cotr: Efficiently bridging cnn and transformer for 3d medical image segmentation. In *Medical Image Computing and Computer Assisted Intervention–MICCAI 2021: 24th International Conference, Strasbourg, France, September 27–October 1, 2021, Proceedings, Part III 24*, pages 171–180. Springer, 2021. [2](#)
- [34] Brandon Yang, Gabriel Bender, Quoc V Le, and Jiquan Ngiam. Condconv: Conditionally parameterized convolutions for efficient inference. *Advances in neural information processing systems*, 32, 2019. [1](#), [2](#), [3](#)
- [35] Jiangning Zhang, Xiangtai Li, Jian Li, Liang Liu, Zhucun Xue, Boshen Zhang, Zhengkai Jiang, Tianxin Huang, Yabiao Wang, and Chengjie Wang. Rethinking mobile block for efficient neural models. *arXiv preprint arXiv:2301.01146*, 2023. [5](#), [6](#), [7](#), [2](#), [3](#), [4](#)
- [36] Tianfang Zhang, Lei Li, Siying Cao, Tian Pu, and Zhenming Peng. Attention-guided pyramid context networks for detecting infrared small target under complex background. *IEEE Transactions on Aerospace and Electronic Systems*, 2023. [5](#), [8](#), [3](#)
- [37] Yundong Zhang, Huiye Liu, and Qiang Hu. Transfuse: Fusing transformers and cnns for medical image segmentation. In *Medical Image Computing and Computer Assisted Intervention–MICCAI 2021: 24th International Conference, Strasbourg, France, September 27–October 1, 2021, Proceedings, Part I 24*, pages 14–24. Springer, 2021. [2](#)
- [38] Yingtao Zhang, Min Xian, Heng-Da Cheng, Bryar Shareef, Jianrui Ding, Fei Xu, Kuan Huang, Boyu Zhang, Chunping Ning, and Ying Wang. Busis: a benchmark for breast ultrasound image segmentation. In *Healthcare*, page 729. MDPI, 2022. [5](#)

# SRSNetwork: Siamese Reconstruction-Segmentation Networks based on Dynamic-Parameter Convolution

## Supplementary Material

### 7. Discription of Dataset

The descriptions of each datasets are as follow:

**Synapse Dataset.** Synapse multi-organ segmentation dataset<sup>1</sup>, used for multi-organ CT segmentation, is from the MICCAI 2015 Multi-Atlas Abdomen Labeling Challenge. It comprises abdominal CT scans of 8 organs from 30 cases (3779 axial images). Each CT volume consists of 85 ~ 198 slices of  $512 \times 512$  pixels, with a voxel spatial resolution of  $([0.54 \sim 0.54] \times [0.98 \sim 0.98] \times [2.5 \sim 5.0])$  mm<sup>3</sup>.

**BUS Dataset.** The Breast UltraSound (BUS) dataset<sup>2</sup> contains 562 breast ultrasound images collected using five different ultrasound devices, including 306 benign cases and 256 malignant cases, each with corresponding ground truth.

**BUSI Dataset.** The Breast UltraSound Images (BUSI) dataset<sup>3</sup> collected from 600 female patients, includes 780 breast ultrasound images, covering 133 normal cases, 487 benign cases, and 210 malignant cases, each with corresponding ground truth labels. Following recent studies [26, 27], we only utilize benign and malignant cases from this dataset.

**TNSCUI Dataset.** The Thyroid Nodule Segmentation and Classification in Ultrasound Images 2020 (TNSCUI) dataset<sup>4</sup> is collected by the Chinese Artificial Intelligence Alliance for Thyroid and Breast Ultrasound (CAAU). It includes 3644 cases of different ages and genders, each with corresponding ground truth labels.

**ISIC 2018 Dataset.** The International Skin Imaging Collaboration (ISIC 2018) dataset<sup>5</sup> contains 2,594 dermoscopic lesion segmentation images.

**SIRST Dataset.** SIRST<sup>6</sup> is a dataset containing 427 images specially constructed for single-frame infrared small target detection, in which the images are selected from hundreds of infrared sequences for different scenarios.

**NUDT-KBT19 Dataset.** The 2019 Aerospace Cup infrared dataset<sup>7</sup>, sponsored by the National University of Defense Technology, contained 5993 infrared images with weak and small targets collected under different meteorological conditions.

### 8. Implement Details

The reconstruction network will be trained first. During the training of the reconstruction network, all data will be unsupervisedly used to train the reconstruction network. To achieve higher performance, additional relevant or irrelevant data can be added. Once the reconstruction network training is complete, we proceed to train the segmentation network, at which point the reconstruction network will not participate in error backpropagation.

### 9. Segmentation performance with different variants of other method

The performance comparison results between our proposed method SRSNet and other state-of-the-art model variants are shown in the Table 8 and Table 9. It can be seen that our proposed method SRSNet achieves best performance.

### 10. Visualization results

We show the more visualization results on seven datasets in Fig. 7 (infrared image), Fig. 8 (CT) and Fig. 9 (Ultrasound and Democapt). Whether in infrared weak image scenarios or medical weak image scenarios, our network has achieved outstanding visual performance. In infrared weak image scenarios, our network detects small targets with higher confidence and integrity (higher value than others), which can be seen in Fig. 7. Also, as shown in Fig. 9, for small lesion images (row 5 and 6), SRSNet gives more accurate spatial localization and lesion shape. Even for challenging examples with low contrast and unclear boundaries (row 1 and 2), SRSNet achieves more complete and convex segmentation results. In addition, for natural light conditions examples (row 3 and 4), our proposed method also achieves more precise edges and shapes.

Moreover, in the task of computed tomography (CT) data segmentation (in Fig. 8), SRSNet has strong ability to distinguish the semantics and it demonstrates more precision organ localization and segmentation.

<sup>1</sup><https://www.synapse.org/#!/Synapse:syn3193805/wiki/217789>

<sup>2</sup><http://cvprp.cs.usu.edu/busbench/>

<sup>3</sup><https://scholar.cu.edu.eg/?q=afahmy/pages/dataset>

<sup>4</sup><https://tn-scui2020.grand-challenge.org/Dataset/>

<sup>5</sup><https://challenge.isic-archive.com/data/#2018>

<sup>6</sup><https://github.com/yimiandai/sirst/tree/master>

<sup>7</sup><http://www.csdata.org/p/387/>

Network	Ultrasound						Dermoscopy	
	BUS (%)		BUSI (%)		TNSCUI (%)		ISIC (%)	
	IOU	F1	IOU	F1	IOU	F1	IOU	F1
MobileViT-xxs [21]	81.62±1.30	89.42±1.10	63.00±3.04	73.71±3.21	70.16±0.15	80.40±0.16	79.76±0.49	87.65±0.43
MobileViT-xs [21]	82.13±1.20	89.69±0.89	63.63±3.54	74.19±3.51	71.13±0.24	81.19±0.20	79.91±0.49	87.73±0.45
MobileViT-s [21]	82.57±1.38	89.99±1.17	64.28±3.78	74.68±3.81	71.64±0.28	81.60±0.25	80.12±0.42	87.89±0.43
EdgeViT-xxs [22]	81.30±1.65	89.12±1.25	61.36±3.25	72.12±3.26	68.36±0.51	78.82±0.5	78.92±0.63	86.97±0.62
EdgeViT-xs [22]	81.86±1.32	89.55±0.95	61.94±3.30	72.58±3.31	69.18±0.26	79.44±0.23	79.17±0.46	87.15±0.46
EdgeViT-s [22]	81.32±1.23	89.13±0.99	61.12±3.69	71.79±4.00	68.74±0.29	79.19±0.36	79.06±0.56	87.06±0.55
RepViT-m1 [30]	76.73±1.12	85.98±0.94	55.52±2.53	67.18±2.73	66.61±0.52	77.48±0.51	78.15±0.60	86.43±0.46
RepViT-m2 [30]	75.93±1.26	85.37±1.07	54.70±2.21	66.27±2.26	64.88±0.87	75.99±0.75	78.03±0.45	86.34±0.47
RepViT-m3 [30]	76.51±1.38	85.79±1.12	56.07±3.51	67.62±3.98	66.21±0.66	77.09±0.49	78.34±0.61	86.62±0.48
EMO-1m [35]	84.68±0.96	91.44±0.72	67.06±3.14	77.11±3.15	73.01±0.46	82.76±0.30	80.97±0.48	88.46±0.35
EMO-2m [35]	85.11±1.10	91.73±0.75	67.90±3.02	77.87±2.96	73.91±0.39	83.39±0.26	81.33±0.35	88.77±0.28
EMO-5m [35]	85.06±0.86	91.66±0.63	68.27±3.32	78.29±3.17	74.34±0.56	83.77±0.45	81.50±0.60	88.90±0.48
EMO-6m [35]	84.89±0.86	91.58±0.63	67.50±4.26	77.71±4.23	74.02±0.39	83.53±0.25	81.31±0.73	88.74±0.57
<b>SRSNet</b>	<b>88.29±0.73</b>	<b>93.44±0.61</b>	<b>74.47±2.23</b>	<b>82.57±2.12</b>	<b>79.33±0.43</b>	<b>87.02±0.33</b>	<b>83.16±0.24</b>	<b>89.72±0.12</b>

Table 8. Different variants of other method result on Ultrasound and Dermoscopy datasets. **val** (bold) : top method.

Network	mIoU↑	Dice↑	HD95↓	Synapse (%)								
				Aorta	Gallbladder	Kidney (L)	Kidney (R)	Liver	Pancreas	Spleen	Stomach	
<i>light-weight natural network</i>												
MobileViT-xxs [21]	38.89	52.58	31.35	23.38	9.52	44.89	43.91	77.01	15.89	57.08	39.48	
MobileViT-xs [21]	40.98	54.73	31.02	23.43	16.69	49.88	47.48	78.65	15.88	56.74	39.10	
MobileViT-s [21]	41.66	55.57	30.81	24.63	16.58	50.94	45.85	77.74	17.90	58.80	40.83	
EdgeViT-xxs [22]	35.93	49.59	36.97	20.93	10.98	38.20	36.97	75.67	14.38	51.78	38.53	
EdgeViT-xs [22]	38.13	51.80	28.71	20.98	12.37	45.93	41.25	77.07	13.93	53.46	40.04	
EdgeViT-s [22]	36.86	50.68	31.82	21.97	12.23	41.42	38.96	76.43	16.00	50.71	37.16	
RepViT-m1 [30]	35.34	49.00	32.71	22.23	6.69	38.27	37.35	75.45	13.80	51.38	37.56	
RepViT-m2 [30]	34.47	47.91	32.26	19.43	7.78	36.69	37.92	74.69	13.01	49.80	36.42	
RepViT-m3 [30]	34.07	47.61	30.69	20.71	7.16	33.56	37.28	74.33	13.28	48.13	38.09	
EMO-1m [35]	45.18	59.35	32.15	28.44	20.67	51.06	48.57	80.23	22.30	59.56	50.61	
EMO-2m [35]	46.53	60.60	32.47	29.15	24.03	50.38	48.89	80.79	23.25	62.80	52.95	
EMO-5m [35]	45.10	59.08	25.00	27.00	21.87	52.57	47.89	79.76	21.93	58.76	51.02	
EMO-6m [35]	45.30	59.47	27.68	28.42	22.85	51.88	48.19	79.50	22.19	60.80	48.54	
<b>SRSNet</b>	<b>69.28</b>	<b>79.80</b>	<b>24.51</b>	<b>80.09</b>	<b>48.97</b>	<b>74.68</b>	<b>71.50</b>	<b>90.80</b>	<b>46.29</b>	<b>80.24</b>	<b>61.71</b>	

Table 9. Different variants of other method result on CT datasets. **val** (bold) : top method

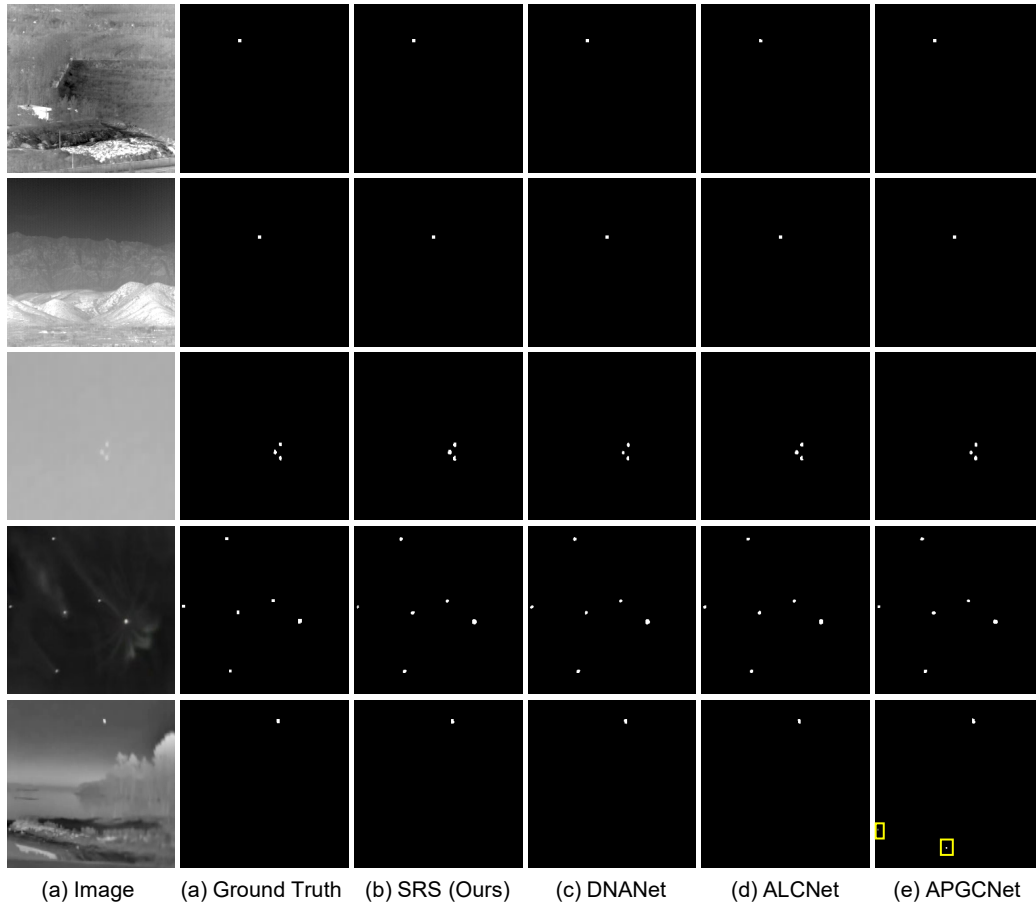


Figure 7. Visualization Results of comparison with DNANet [16], ALCNet [10] and APGCNet [36] on infrared image dataset. Row 1, 2 NUDT - KBT2019 samples, Row 3, 4 and 5 - SIRST samples. Yellow boxes represent error segmentation.

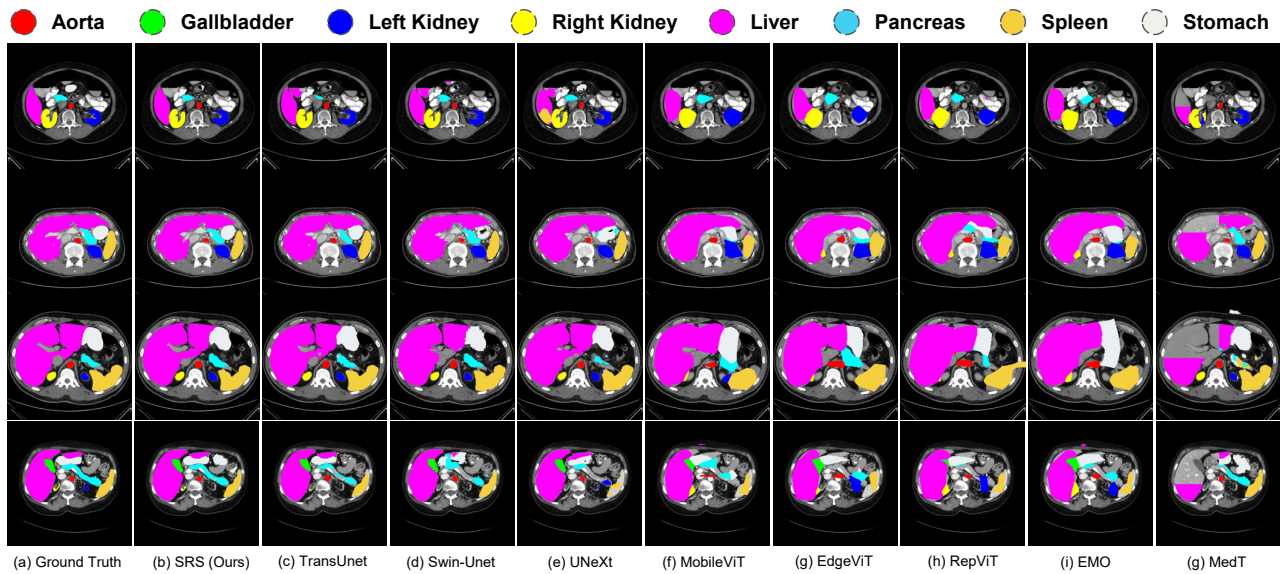


Figure 8. Visualization Results of comparison with TransUnet [7], Swin-Unet [6], UNeXt [27], MobileViT [21], EdgeViT [22], RepViT [30], EMO [35] and MedT [28] on CT Dataset.

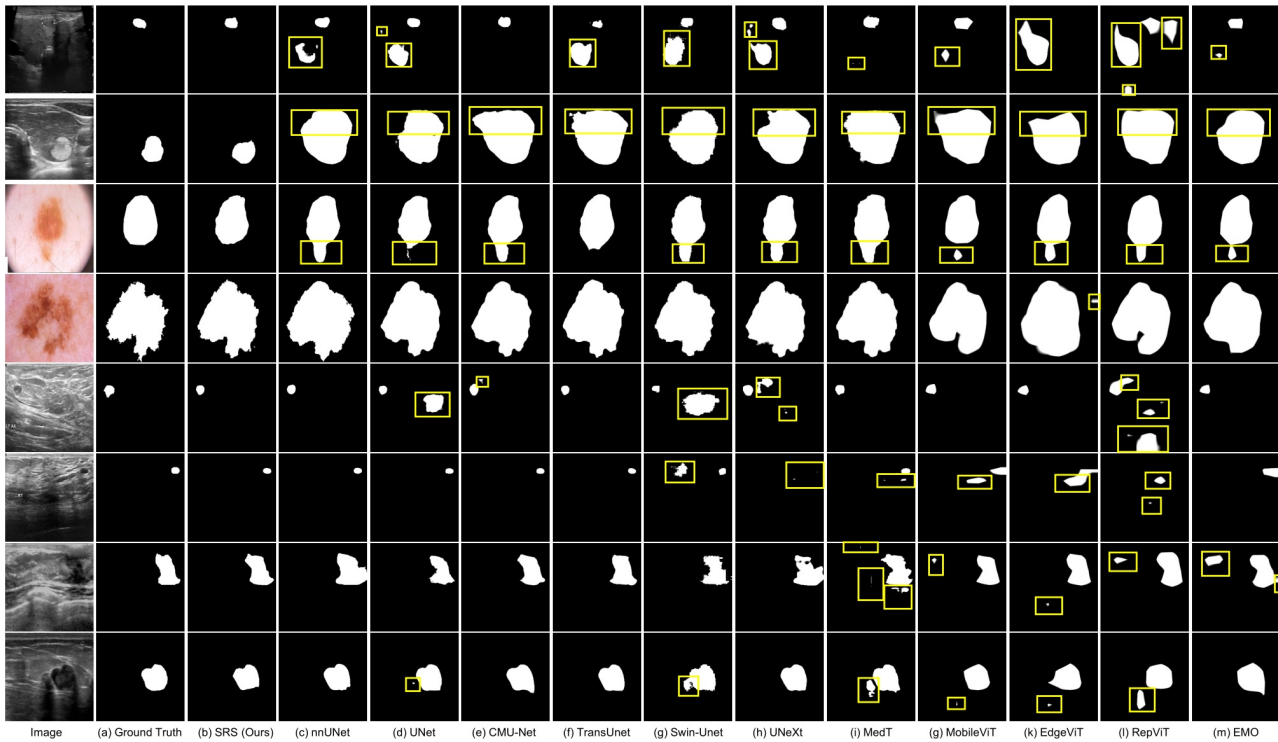


Figure 9. Visualization Results of comparison with nnUnet [14], UNet [24], CMU-Net [26], TransUnet [7], Swin-Unet [6], UNeXt [27], MedT [28], MobileViT [21], EdgeViT [22], RepViT [30] and EMO [35] on Ultrasound and Dermocapte Dataset. Row 1 and 2 - TNSCUI samples, Row 3 and 4 - ISIC18 samples, Row 5 and 6 – BUSI samples, Row 7 and 8 - BUS samples. Yellow boxes represent error segmentation.